LLNL-JRNL-408798

Enthalpy Diffusion in Multicomponent Flows

A. W. Cook

November 18, 2008

Physics of Fluids

Enthalpy Diffusion in Multicomponent Flows

Andrew W. Cook

Lawrence Livermore National Laboratory, Livermore, CA 94551-0808;

awcook@llnl.gov

Abstract

The enthalpy diffusion flux in the multicomponent energy equation is a well known yet frequently neglected term. It accounts for energy changes, associated with compositional changes, resulting from species diffusion. Enthalpy diffusion is important in flows where significant mixing occurs between species of dissimilar molecular weight. The term plays a critical role in preventing local violations of the entropy condition. In simulations of nonpremixed combustion, omission of the enthalpy flux can lead to anomalous temperature gradients, which may cause mixing regions to exceed ignition conditions. The term can also play a role in generating acoustic noise in turbulent mixing layers. Euler solvers that rely on numerical diffusion to mix fluids cannot accurately predict the temperature in mixed regions. On the other hand, Navier-Stokes solvers that incorporate enthalpy diffusion can provide much more accurate results.

Preprint submitted to Physics of Fluids *11 November 2008*

1 Introduction

Turbulent mixing of dissimilar fluids is ubiquitous in combustion devices, Inertial Confinement Fusion (ICF) experiments, astrophysical events, atmospheric flows and a host of other applications. In developing Computational Fluid Dynamics (CFD) codes for such processes, choices must be made as to which terms to include in the governing equations. Choosing the bare minimal set results in so-called Euler solvers, wherein viscous, conductive and diffusive terms are all neglected. Euler solvers have been widely used to study molecular mixing in turbulent flows such as Rayleigh-Taylor [1] and Richtmyer-Meshkov [2] instabilities. The Euler equations however, do not actually admit molecular mixing. Such simulations rely on numerical diffusion to effectively mix the various fluid species at the grid scale.

Euler solvers are cheap; however, they are notorious for generating spurious oscillations at material interfaces [3, 4]. The well-known problem occurs in conservative formulations, as a result of the averaging process, when the temperature, T, and ratio of specific heats, γ, vary across the interface [5]. There is also, however, a less well-known problem that occurs with fluids of different molecular weight, even if T and γ are constant across the interface. The problem arises from the fact that as species diffuse, they carry their energy, as well as their mass, along with them. Hence numerical diffusion, which mixes masses, must be accompanied by an enthalpy flux, otherwise the internal energy of the mixture will not properly adjust to changes in composition. In the full multicomponent Navier-Stokes equations, the so-called enthalpy diffusion term ensures consistency between mass and energy diffusion.

In constructing Navier-Stokes codes for turbulent mixing, it is common practice to first build a single-fluid flow solver and then extend it to the case of multiple species. Sometimes this is accomplished by simply adding a species advection-diffusion equation, while leaving the single-fluid versions of the mass, momentum and energy equations unchanged. As with Euler codes, this practice fails to account for enthalpy diffusion effects. Although flow assumptions can vary for different applications, a brief literature survey reveals that a large number of multicomponent Navier-Stokes simulations omit the enthalpy diffusion term in the energy equation [6, 7, 8, 9, 10, 11]. The primary objective of this paper is to demonstrate some of the errors that can result from neglecting this term and to provide some guidance as to when it ought to be included.

The organization of this paper is as follows. In Section 2 the governing equations for multicomponent flows are introduced and issues relating to turbulence modeling are addressed. In Section 3 a simple gedanken experiment is presented, which illustrates the role of the enthalpy diffusion term in preserving the second law of thermodynamics. Section 4 gives results of simulations with and without enthalpy diffusion for a Kelvin-Helmholtz (KH) instability, a shock bubble interaction and a Rayleigh-Taylor (RT) instability. Conclusions are given in Section 5. Appendix A describes details of the numerical algorithm and Appendix B provides a recipe for computing the enthalpy diffusion term, given a tabular equation of state.

2 Governing Equations

2.1 Conservation Laws

In single-fluid flows, conservation of mass, momentum and energy is expressed by the Navier-Stokes equations:

$$\frac{\partial \rho}{\partial t} + \nabla \cdot (\rho \mathbf{u}) = 0 \ , \tag{1}$$

$$\frac{\partial \rho \mathbf{u}}{\partial t} + \nabla \cdot (\rho \mathbf{u}\mathbf{u} + p\underline{\boldsymbol{\delta}}) = \nabla \cdot \underline{\boldsymbol{\tau}} \ , \tag{2}$$

$$\frac{\partial E}{\partial t} + \nabla \cdot [(E + p)\mathbf{u}] = \nabla \cdot (\underline{\boldsymbol{\tau}} \cdot \mathbf{u} - \mathbf{q_c}) \ , \tag{3}$$

where ρ is density, $\mathbf{u}$ is velocity, p is pressure, $\underline{\boldsymbol{\delta}}$ is the unit tensor, $\underline{\boldsymbol{\tau}}$ is the viscous stress tensor, E is total energy and $\mathbf{q_c}$ is heat conduction. The total energy is

$$E = \rho \left(e + \frac{\mathbf{u} \cdot \mathbf{u}}{2} \right) \ , \tag{4}$$

where e represents internal energy. For Newtonian fluids, the viscous stress tensor is

$$\underline{\boldsymbol{\tau}} = \mu(2\underline{\mathbf{S}}) + (\beta - \frac{2}{3}\mu)(\nabla \cdot \mathbf{u})\underline{\boldsymbol{\delta}} \ , \tag{5}$$

where μ is dynamic (shear) viscosity, β is bulk viscosity and $\underline{\mathbf{S}}$ is the symmetric strain rate tensor,

$$\underline{\mathbf{S}} = \frac{1}{2}[\nabla \mathbf{u} + (\nabla \mathbf{u})^{\dagger}] \ , \tag{6}$$

where $(\nabla \mathbf{u})^\dagger$ denotes the transpose of the dyadic $\nabla \mathbf{u}$. The conductive heat flux is described by Fourier's law,

$$\mathbf{q_c} = -\kappa \nabla T \ , \tag{7}$$

where κ is thermal conductivity and T is temperature. For ideal gases,

$$p = (\gamma - 1)\rho e \ , \tag{8}$$

where $\gamma = c_p/c_v$ is the ratio of specific heats. Equations (1), (2), (3) and (8) adequately describe a wide variety of flow phenomena, including shocks, turbulence, boundary layers, sound waves, heat transport etc. Numerous flow solvers are based on these equations, sometimes with additional terms for buoyancy or other physics.

In order to treat mixing in flows involving more than one fluid, (1)-(3) are often supplemented with an advection-diffusion equation for $N-1$ species, where N is the total number of fluids present. This additional equation takes the form

$$\frac{\partial \rho Y_i}{\partial t} + \nabla \cdot (\rho Y_i \mathbf{u}) = \nabla \cdot (-\mathbf{J}_i) \ , \tag{9}$$

where Y_i is the mass fraction of species i and $\mathbf{J}_i$ is its diffusive mass flux. The diffusional fluxes are commonly computed via the Fickian diffusion approximation,

$$\mathbf{J}_i \approx -\rho \left(D_i \nabla Y_i - Y_i \sum_{j=1}^{N} D_j \nabla Y_j \right) \ , \tag{10}$$

where D_i is a species diffusion coefficient. In this approximation, pressure and temperature (Soret) forces are neglected and the multicomponent fluid is regarded as a binary mixture of species i and a complementary composite species composed of all other materials. The last term in (10) ensures that $\sum_{i=1}^{N} \mathbf{J}_i = 0$, which is necessary in order to recover (1) when (9) is summed over all species. After solving (9) for $N-1$ fluids, the Nth fluid can then be obtained from the relation $\sum_{i=1}^{N} Y_i = 1$. Alternatively, (9) can be solved for all N fluids, which removes the need for (1).

When molecules of two different gases diffuse into each other, they carry along their energy as well as their mass. Hence, changes in composition are accompanied by changes in the internal energy (e) of the mixture. Thus, the correct form of the energy equation for multicomponent flows is

$$\frac{\partial E}{\partial t} + \nabla \cdot [(E+p)\mathbf{u}] = \nabla \cdot \left(\underline{\boldsymbol{\tau}} \cdot \mathbf{u} - \mathbf{q_c} - \mathbf{q_d}\right) , \tag{11}$$

where

$$\mathbf{q_d} = \sum_{i=1}^{N} h_i \mathbf{J}_i \tag{12}$$

is the interdiffusional enthalpy flux [12, 13, 14, 15]. The enthalpy of each individual species is defined as

$$h_i = e_i + p_i/\rho_i , \tag{13}$$

where e_i, p_i and ρ_i are species internal energy, species pressure and species density, respectively. Radiative heat transport as well as the diffusion-thermo (Dufour) effect have been neglected in (11).

2.2 Turbulence Modeling

In Direct Numerical Simulations (DNS), length and time scales are small, such that molecular viscosity, diffusivity and conductivity play important roles. Diffusion of momentum, materials and heat is captured by the terms on the right-hand sides of (2), (9) and (11). In Large-Eddy Simulations (LES), Reynolds numbers can be large, such that turbulent diffusion at the grid scale dwarfs molecular diffusion. In such cases, subgrid-scale models, similar or identical in form to the terms on the right-hand sides, are typically introduced in order to provide stability and to model the influence of unresolved scales on the resolved flow. In Reynolds-Averaged Navier-Stokes (RANS) simulations, turbulence models, similar or identical in form to the RHS terms, are also introduced, in order to capture the effects of turbulent fluctuations on the ensemble-averaged flow. Regardless of the type of simulation being performed, the presence of a diffusive mass flux in (9) necessitates the presence of an enthalpy flux in (11); otherwise, the internal energy in grid cells containing more than one species will not be properly adjusted for changes in composition. In other words, if $\mathbf{J}_i$ is nonzero, then $\mathbf{q_d}$ is potentially important, regardless of whether $\mathbf{J}_i$ represents a molecular (DNS), subgrid-scale (LES) or turbulent diffusion (RANS) flux. The numerical simulations presented herein are of the LES variety; nevertheless, the results apply equally well to DNS, as well as RANS calculations.

3 Thermodynamic Considerations

The importance of the enthalpy diffusion term can be illustrated through a simple gedanken experiment. Consider two ideal gases, with constant specific heats, placed side by side in pressure and temperature equilibrium. The gases have the same γ but different molecular weights. The gases are quiescent and nonconducting but undergo diffusion. In the single fluid approximation, all terms in (1), (2) and (3) are zero; hence, ρ, $\mathbf{u}$, e and p remain constant in time. The temperature, however, must evolve along with changes in composition; i.e., if Y_L and Y_H are the mass fractions of the light and heavy gases, respectively, then

$$T = \frac{e}{c_v} = \frac{e}{Y_L c_{v,L} + Y_H c_{v,H}} \ , \tag{14}$$

where $c_{v,L}$ and $c_{v,H}$ are the light and heavy specific heats at constant volume. The specific heats are related by

$$M_L c_{v,L} = M_H c_{v,H} \ , \tag{15}$$

where M_L and M_H are the light and heavy molecular weights. If T_o is the initial temperature throughout the domain, then the temperature, at some later time, in the region originally occupied by the light gas (left-hand side) is

$$T^{<} = \frac{T_o}{Y_L + Y_H M_L / M_H} \ ; \tag{16}$$

similarly,

$$T^{>} = \frac{T_o}{Y_L M_H / M_L + Y_H} \tag{17}$$

is the temperature in the region initially occupied by the heavy gas (right-hand side). As time progresses, the temperature in the left-hand region ($^<$) increases, while the temperature in the right-hand region ($^>$) decreases. Such a spontaneous generation of a temperature gradient is contrary to every day experience, except in July when you leave your car in the parking lot.

The impossibility of the above scenario can be understood by examining the entropy of the system. Taking the initial temperature, T_o, and the initial pressure, p_o, as reference values, the specific entropy of the mixture is

$$s = c_p \ln(T/T_o) - R \ln(p/p_o) - R \left[X_L \ln(X_L) + X_H \ln(X_H) \right] \ , \tag{18}$$

where

$$c_p = Y_L c_{p,L} + Y_H c_{p,H} \ , \tag{19}$$

is the constant-pressure specific heat of the mixture,

$$R = R_u/M \ , \tag{20}$$

is the apparent gas constant (R_u being the universal gas constant), $X_L = Y_L M/M_L$ is the mole fraction of light gas, $X_H = Y_H M/M_H$ is the mole fraction of heavy gas and

$$M = \frac{1}{Y_L/M_L + Y_H/M_H} = X_L M_L + X_H M_H \tag{21}$$

is the mixture molecular weight. The last (bracketed) term in (18) is the specific entropy of mixing, which is zero for the segregated initial state. Letting m_L and m_H denote the masses of the light and heavy fluids, respectively

($m = m_L + m_H$ being the total mass), the total entropy of the system is

$$\mathcal{S} = m_L s^< + m_H s^> \ , \tag{22}$$

where $s^<$ and $s^>$ are the respective specific entropies in the left and right regions. The total entropy is initially zero, since no mixing has occurred and the gases are at their reference state. In the final equilibrium state, once diffusion has run its course and the mass fractions are uniform throughout the domain, the specific entropy in the two regions is

$$s_f^< = c_{p,f} \ln(T_f^</T_o) - R_f \left[(V_L/V)\ln(V_L/V) + (V_H/V)\ln(V_H/V)\right] \tag{23}$$

$$s_f^> = c_{p,f} \ln(T_f^>/T_o) - R_f \left[(V_L/V)\ln(V_L/V) + (V_H/V)\ln(V_H/V)\right] \ , \tag{24}$$

where f subscripts denote final equilibrium values for composition-dependent quantities, V_L is the volume of light fluid, V_H is the volume of heavy fluid and $V = V_L + V_H$ is the total volume. Plugging (16) and (17) into (23) and (24), and using the relations

$$c_p = \frac{\gamma R}{\gamma - 1} \ , \tag{25}$$

$$\frac{V_i}{V} = \frac{M Y_i}{M_i} \ , \tag{26}$$

yields

$$s_f^< = -R_f \left[\frac{\gamma}{\gamma - 1} \ln(M_L/M) + \sigma\right] \ , \tag{27}$$

$$s_f^> = -R_f \left[\frac{\gamma}{\gamma - 1} \ln(M_H/M) + \sigma\right] \ , \tag{28}$$

where

$$\sigma \equiv (V_L/V)\ln(V_L/V) + (V_H/V)\ln(V_H/V) < 0 \ . \tag{29}$$

The total entropy can be expressed in terms of volume and molecular weight ratios by writing the mass of each fluid as

$$m_i = \frac{M_i V_i}{MV} m \ . \tag{30}$$

The maximum entropy of mixing occurs when $V_L = V_H$, for which $M = (M_L + M_H)/2$, $m_i = mM_i/(2M)$ and $\sigma = -\ln(2)$. For nobel gases ($\gamma = 5/3$) of equal volumes, any ratio of molecular weights (M_H/M_L) above 5.845 will result in a decrease in total entropy ($\Delta\mathcal{S} = \mathcal{S}_f - \mathcal{S}_o < 0$), which violates the second law of thermodynamics. Smaller molecular weight ratios can also violate the second law, depending on the gas volumes present. In reality, the correct change in total entropy ought to simply be the entropy of mixing,

$$\Delta\mathcal{S} = -mR_f\sigma > 0 \ , \tag{31}$$

which satisfies the second law, regardless of the molecular weights.

Now consider what physically must take place in the experiment. Once the diffusion process is complete and the system has reached equilibrium, the number-density of molecules will be the same as it was initially. This is a consequence of the fact that the mean free path of the molecules is large compared to their size; hence, the molecules can be treated as independent of one another. This gives rise to the Amagat-Leduc law, which for our case states that

$$\frac{1}{\rho} = \frac{Y_L}{\rho_L} + \frac{Y_H}{\rho_H} \ , \tag{32}$$

where the constant densities of the light and heavy fluids, ρ_L and ρ_H, are related by

$$\frac{\rho_L}{M_L} = \frac{\rho_H}{M_H} \ . \tag{33}$$

Since the mass fractions become constant throughout the domain ($Y_{L,f}^{<} = Y_{L,f}^{>}$ & $Y_{H,f}^{<} = Y_{H,f}^{>}$), the mixture density must also relax from a discontinuous jump at the interface to a constant value everywhere. It is tempting to think of this density relaxation process as diffusion phenomenon; however, density does not diffuse. A brief glance at the continuity equation (1) reveals that ρ can only change if $\mathbf{u}$ is finite ($\nabla \cdot \mathbf{u} \neq 0$ in this 1-dimensional case). A further glance at the momentum equation (2) reveals that $\mathbf{u}$ can only become finite if there is a nonzero pressure gradient. Rewriting (11) in terms of pressure and enthalpy yields

$$\frac{Dp}{Dt} = \rho \frac{Dh}{Dt} + \nabla \cdot (\mathbf{q_c} + \mathbf{q_d}) - \underline{\boldsymbol{\tau}} : \nabla \mathbf{u} \ , \tag{34}$$

where $h = e + p/\rho$ is the enthalpy of the mixture. By examining (34) it becomes clear that, for nonconducting gases, $\mathbf{q_d}$ is the only term capable of disturbing the initial pressure field. The pressure imbalance generated by the enthalpy diffusion term causes a divergence in the velocity field, which in turn, serves to relax the density gradient. In this manner, the enthalpy diffusion term helps preserve the entropy constraint.

4 Results

In order to quantify the importance of the enthalpy diffusion term in simulations of turbulent mixing, we use a low-dissipation numerical algorithm consisting of a tenth-order centered compact scheme for spatial derivatives, combined with fourth-order Runge-Kutta (RK) integration. Molecular viscosity, conductivity and species diffusivities are supplemented with fourth-order grid-dependent components, which ensure that all flow variables remain smooth with respect to the grid scale. The simulations are of the LES variety, with the grid-dependent viscosity, conductivity and species diffusivities functioning effectively as subgrid-scale models. The numerical method is described in detail in Appendix A.

As a first example of what can go wrong by neglecting $\mathbf{q_d}$, we consider a two-dimensional hydrogen-air shear layer, typical of combustion applications. The domain is discretized onto a 512×512 grid with 1 mm spacing. The flow is initialized at atmospheric pressure with a temperature of 600 K. The streams of H_2 and air flow in opposite directions at speeds of 100 m/s. Small-amplitude broad-banded perturbations are applied at the interface between the two gas streams. Two identical simulations were run (same perturbations etc.) the first with the enthalpy diffusion term neglected (3) and the second with it included (11). Results are shown in Figs. 1, 2 and 3. Fig. 1 shows three snapshots of the density field from each simulation. Although the flows start out identically, they rapidly decorrelate.

Fig. 2 displays the temperature fields corresponding to the snapshots in Fig. 1. At 1 ms, cooling on the air (upper) side of the interface and heating on

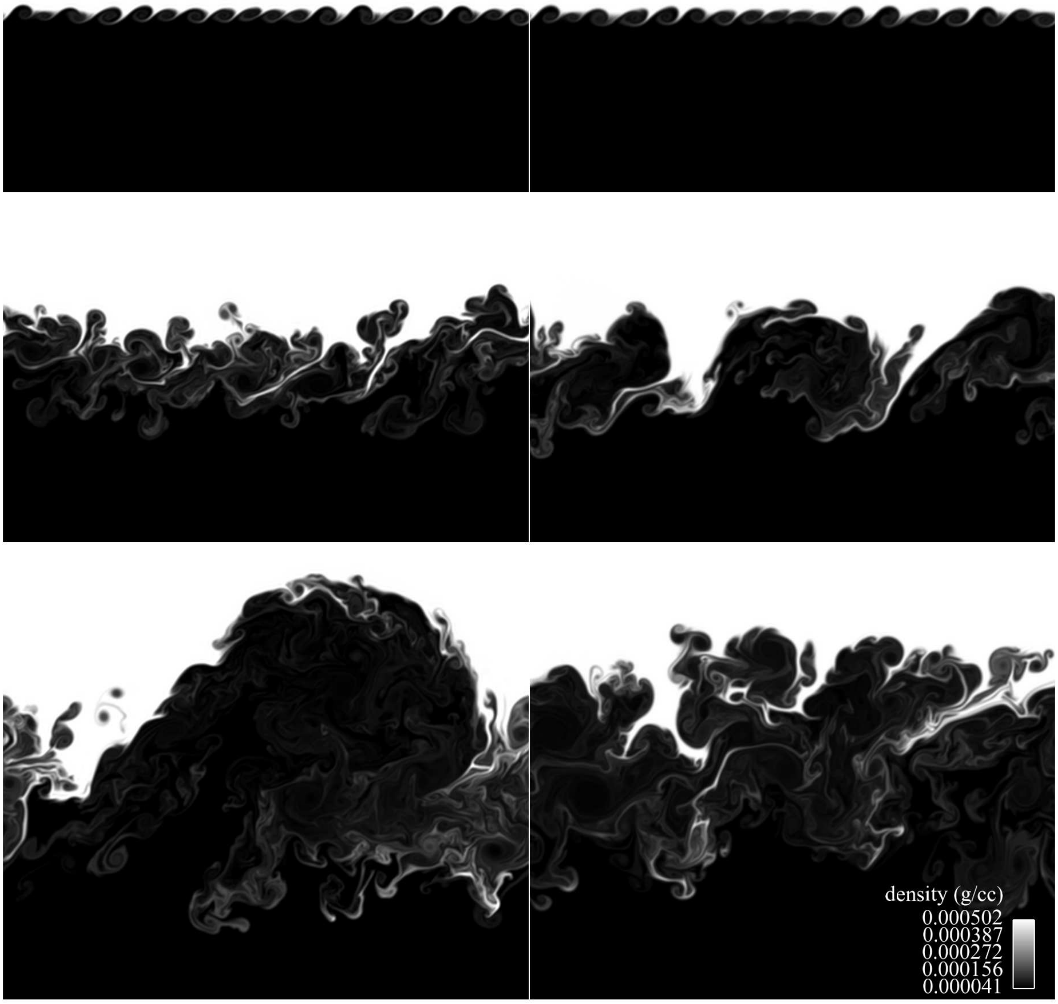

Fig. 1. Density at 1 (top), 5 (middle) and 10 ms (bottom) from simulations of a hydrogen-air shear layer, neglecting (left) and including (right) the enthalpy diffusion term. Hydrogen (black) is on the bottom and flowing to the left, whereas air (white) is on the top and flowing to the right.

the hydrogen side (lower) are clearly visible. This is in agreement with the results of the gedanken experiment. At 10 ms, temperature variations in the simulation with enthalpy diffusion are small, i.e., $592\,\mathrm{K} < T < 601\,\mathrm{K}$. By

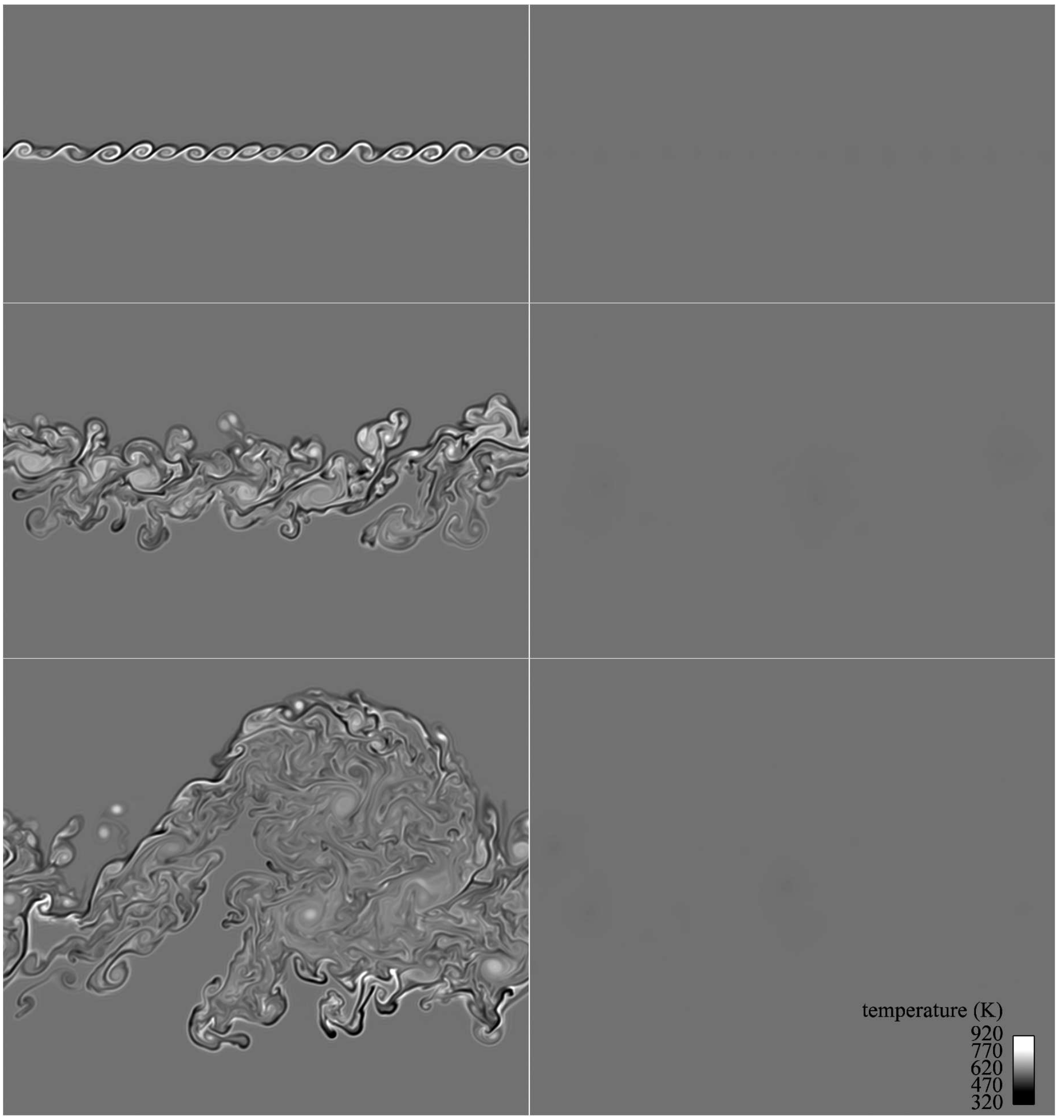

Fig. 2. Temperature at 1 (top), 5 (middle) and 10 (bottom) ms for hydrogen-air shear layer. Plots on the left/right are with the enthalpy diffusion term excluded/included. White regions exceed the ignition temperature.

contrast, the minimum and maximum temperatures in the simulation without enthalpy diffusion are 315 K and 924 K, respectively. The ignition temperature of hydrogen at atmospheric pressure is 853 K.

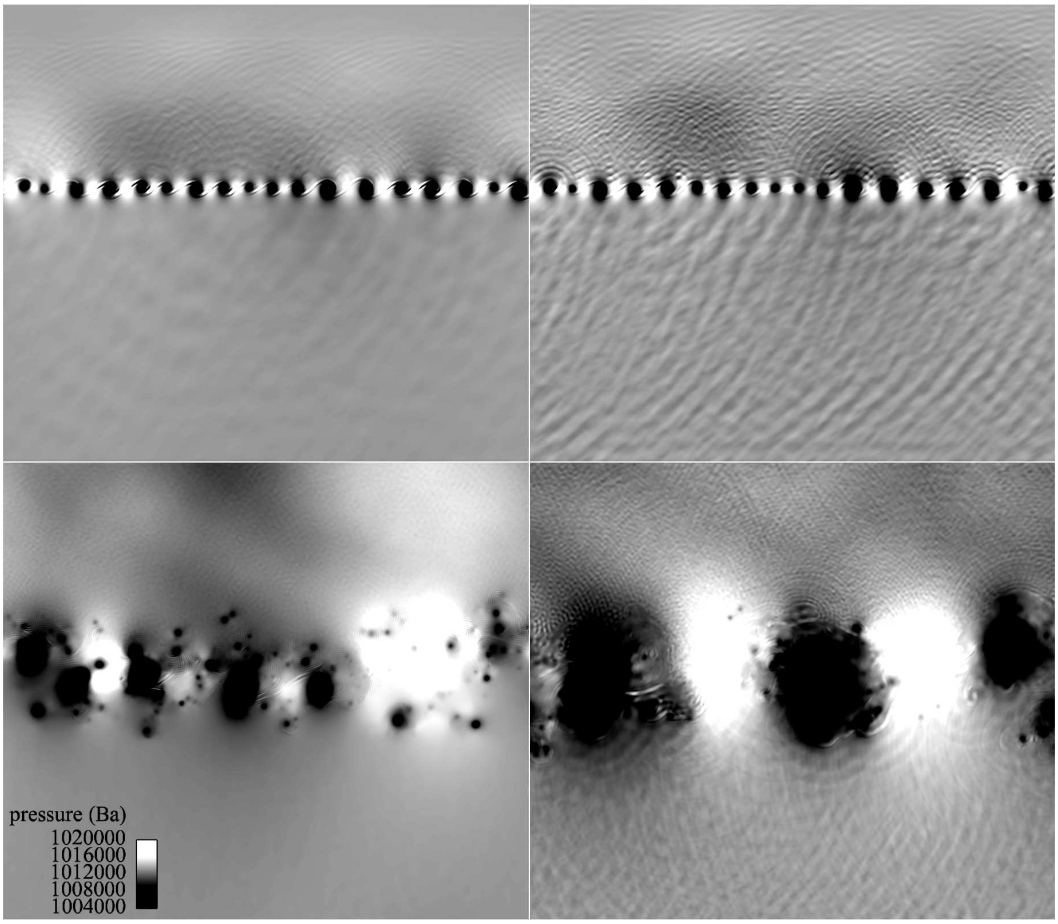

Fig. 3. Pressure at 1 (top) & 5 (bottom) ms in hydrogen-air shear layer without (left) and with (right) enthalpy diffusion.

Fig. 3 shows the pressure field for the shear layer. Acoustic waves are clearly visible emanating from the mixing region. The sound waves are much more pronounced in the simulation with enthalpy diffusion. This stand to reason, since the gedanken experiment showed that the enthalpy diffusion term perturbs the pressure field. As turbulent eddies strain the interface, large species-diffusion fluxes ($\mathbf{J}_i$) are generated at small scales. The enthalpy diffusion associated with these fluxes generates localized pressure oscillations, which radiate out from the mixing region as sound waves. Without these enthalpy fluxes, the acoustic field is suppressed. Sound waves are generally regarded as unimportant in low Mach number combustion applications; nevertheless, they prevent entropy violations by providing the expansion/compression mechanism that keeps temperatures in check.

As a second example to elucidate the effects of enthalpy diffusion, we consider the shock bubble experiment of Haas and Sturtevant [16]. The initial conditions are depicted in Fig. 4. They consist of a Mach 1.22 shock in air, located 50 mm from the center of a cylindrical helium bubble of radius 25 mm. The grid resolution is 0.056 mm, the same as in the simulations by Quirk and Karni [17] and Marquina and Mulet [4].

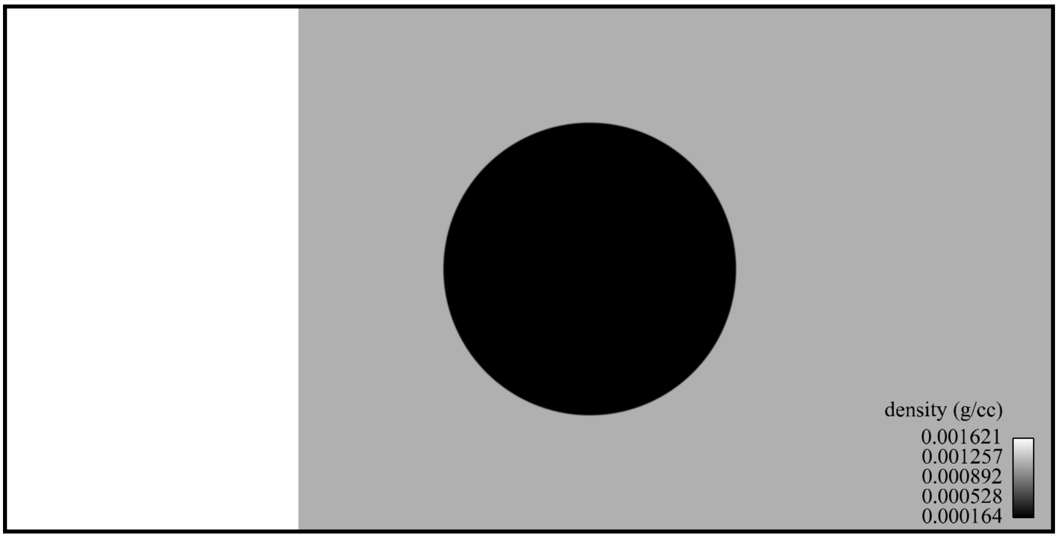

Fig. 4. Initial density field for simulation of Haas-Sturtevant experiment. A Mach 1.22 shock in air (left) impacts a cylindrical helium bubble of diameter 50 mm (center). The shock is initially 50 mm from the center of the bubble.

Figure 5 shows the temperature field at various times from the simulations neglecting and including enthalpy diffusion. Once again, much larger temperature variations are present in the simulation neglecting $\mathbf{q_d}$. The helium side of the bubble interface is hot, whereas the air side is cold. By including $\mathbf{q_d}$, the anomalous temperature gradients in the diffusion regions disappear.

In addition to the temperature field, it is interesting to examine the effects of enthalpy diffusion on the density field as well. Recall that in the gedanken experiment without enthalpy diffusion, the density discontinuity remained undisturbed. Figure 6 compares density at 500 ms on zoomed-in regions from each simulation. Close examination of the images reveals that the density field in the simulation with enthalpy diffusion is smoother. This fits in with the results of the gedanken experiment, where the enthalpy diffusion term was ultimately responsible for relaxing the density discontinuity. It would be wrong to say that the density field in the right image is more diffuse. There is no diffusion term in the continuity equation (1). Smoothing of the density field is brought about by a local divergence in the velocity field, which is here influenced by both $\mathbf{q_c}$ and $\mathbf{q_d}$.

As a third and final example of the importance of enthalpy diffusion, we consider the high-energy Rayleigh-Taylor configuration of Dimonte and Tipton [8]. We employ deuterium-tritium (DT) and tin (Sn) for the light and heavy species, respectively, since these materials are relevant to ICF applications. Gravity is incorporated by adding $\rho\mathbf{g}$ and $\rho\mathbf{g}\cdot\mathbf{u}$ to the right-hand sides of (2) and (11), respectively, where $\mathbf{g} = (0, 0, -9.8 \times 10^{-4})\mathrm{cm}/\mu\mathrm{s}^2$. The computational domain consists of a 1 cm^2 box with a grid resolution of 0.01 mm. The ambient temperature is set to 1 eV, which, as pointed out by Dimonte and Tipton, is hot enough to make the initial density profile nearly flat. The densities of the DT and Sn, on either side of the interface, are 0.520 and 7.33 g/cm^3, respectively, which corresponds to an Atwood number, $(\rho_H - \rho_L)/(\rho_H + \rho_L)$, of 0.87. For this case, we used a tabular equation of state, together with the pressure/temperature equilibration algorithm described in Appendix B.

Figure 7 depicts the evolution of the density field for the two simulations. As with the Kelvin-Helmholtz case, the flows start out identically but soon become completely decorrelated. Temperature is displayed in Fig. 8, where once again, large gradients are observed in the simulation neglecting the enthalpy diffusion term. In the simulation with enthalpy diffusion, the temperature varies by less than 5.2×10^{-3} eV; whereas, in the simulation without enthalpy diffusion, the temperature ranges from 0.5 to 2 eV. Such factor-of-two errors ought to cause serious concern in evaluating reaction rates or other temperature-sensitive quantities.

The acoustic field is manifest in Fig. 9, which shows velocity dilatation for each RT simulation. Recall from the gedanken experiment that enthalpy diffusion generates pressure gradients, which in turn, cause divergence of the velocity field. Hence, the simulation incorporating $\mathbf{q_d}$ should be expected to exhibit a stronger acoustic field. This is exactly what is seen in Fig. 9; i.e., the sound waves emanating from the mixing layer are much stronger in the simulation with enthalpy diffusion.

It should be noted that our simulations are two-dimensional LES, whereas Dimonte and Tipton performed one-dimensional RANS simulations with the K-L turbulence model [8]. RANS models such as K-L are designed to produce t^2 growth of RT mixing regions. Hence the turbulent (RANS) diffusion (analogous to the $\mathbf{J}_i$ term), in this case, must be much larger than the Fickian (LES) diffusion, which produces $t^{1/2}$ growth of interfaces. It seems likely therefore, that $\mathbf{q_d}$ would be larger in the RANS case than in the LES (or DNS) case.

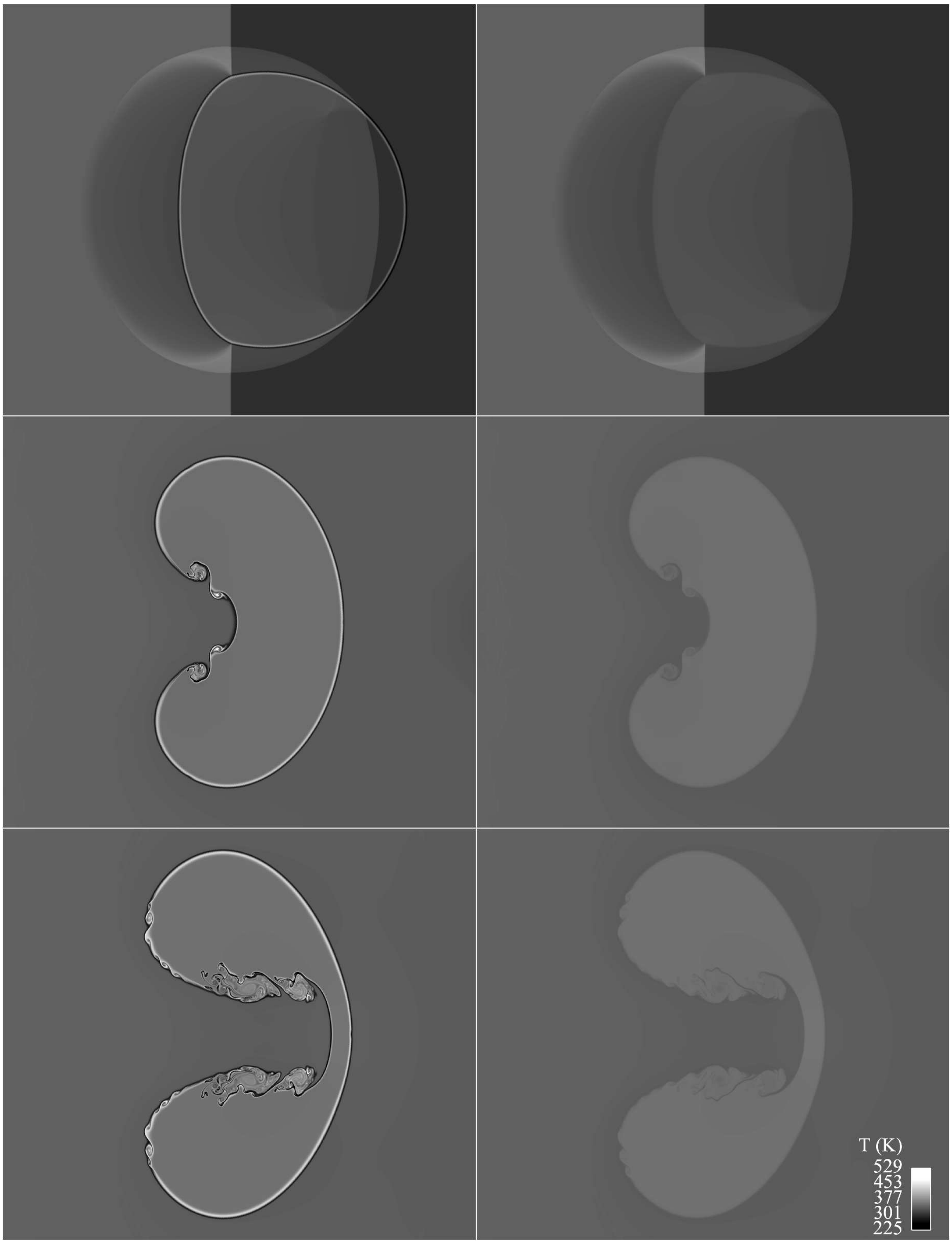

Fig. 5. Temperature at 100 (top), 300 (middle) & 500 (bottom) ms from shock-bubble simulations neglecting (left) and including (right) enthalpy diffusion.

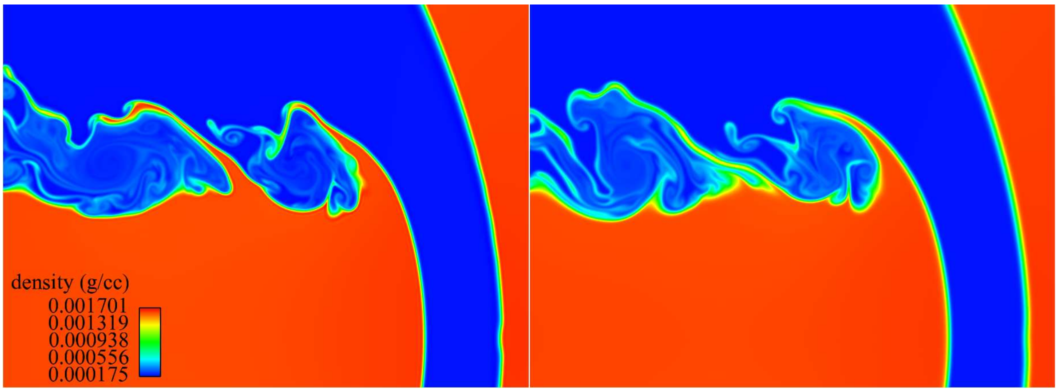

Fig. 6. Density at 500 ms from shock-bubble simulations excluding (left) and including (right) enthalpy diffusion.

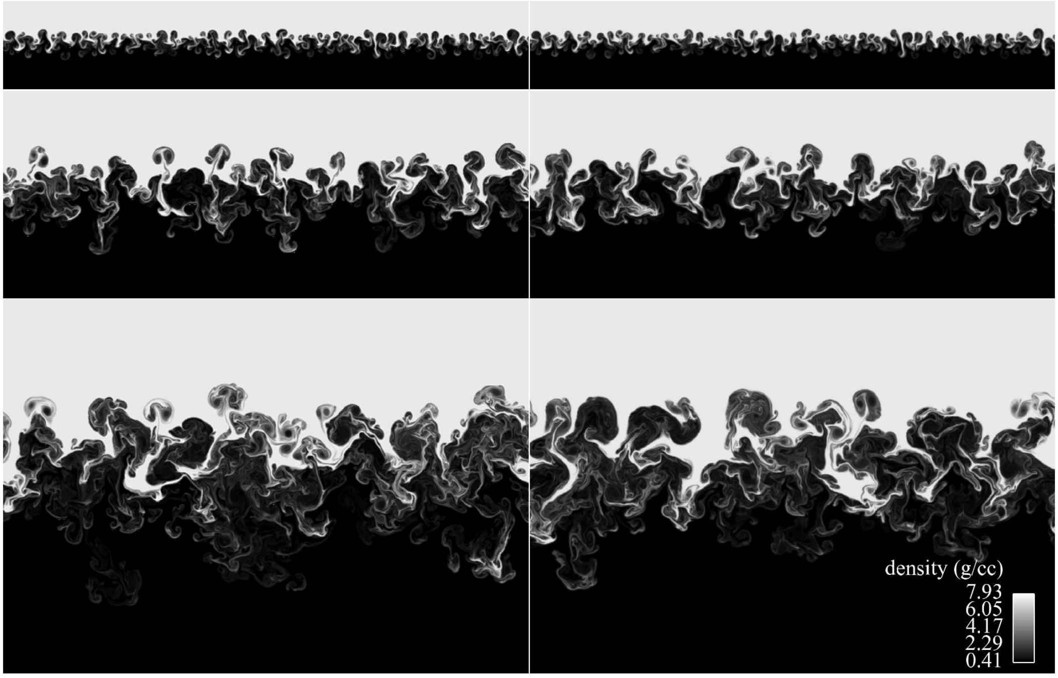

Fig. 7. Density at 20 (top), 40 (middle) & 60 (bottom) ms from Rayleigh-Taylor simulations neglecting (left) and including (right) enthalpy diffusion. The upper fluid is tin (Sn) and the lower fluid is deuterium-tritium (DT).

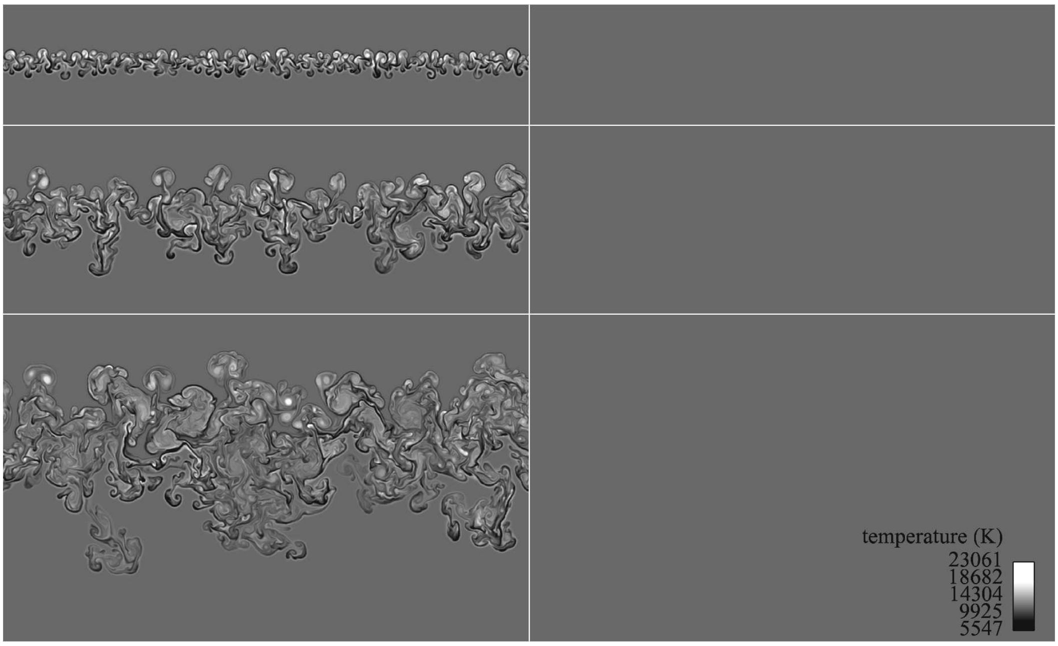

Fig. 8. Temperature at 20 (top), 40 (middle) & 60 (bottom) ms from Rayleigh-Taylor simulations neglecting (left) and including (right) enthalpy diffusion.

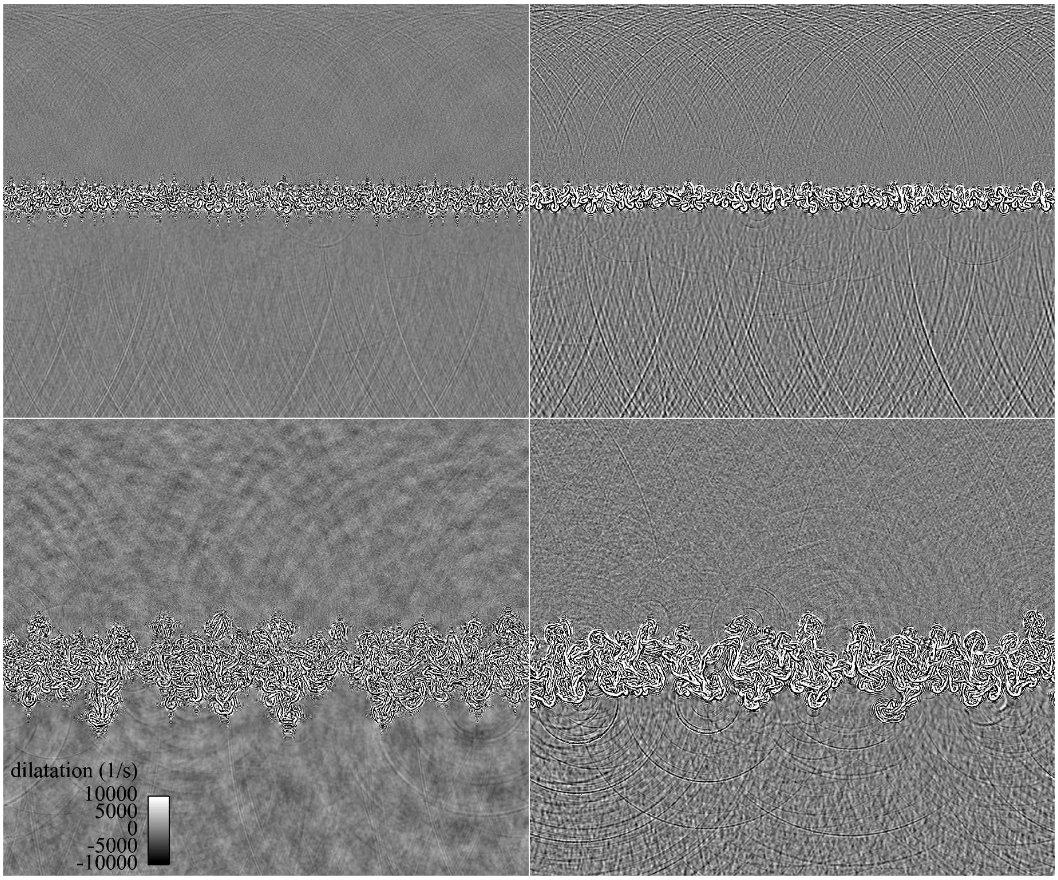

Fig. 9. Velocity divergence at 20 (top) and 40 (bottom) ms from Rayleigh-Taylor simulations neglecting (left) and including (right) enthalpy diffusion.

5 Conclusions

Enthalpy diffusion can play several critical roles in multicomponent flows involving miscible fluids, especially when differences in molecular weights are large. The term prevents entropy violations by reducing temperature gradients in mixing regions. Anomalous temperatures can be generated if the term is neglected, which can lead to premature ignition or extinction of diffusion flames. Enthalpy diffusion also generates pressure pulses at highly strained material interfaces. These pulses can appear as sound waves emanating from turbulent mixing layers. The term is furthermore responsible for smoothing density gradients in diffusion regions by indirectly causing local dilatations of the velocity field.

Euler solvers that rely on numerical diffusion to mix fluids are incapable of predicting accurate temperatures in mixing regions. In fact, if differences in molecular weights are large, then any multicomponent simulation that neglects the enthalpy diffusion term will potentially exhibit large errors in the temperature field. Errors in other flow variables may also be present to a lesser extent. Considering the low computational cost of the term (it requires no additional derivatives) it seems prudent to include it whenever mass diffusion is present ($\mathbf{J}_i \neq 0$) in the species transport equation.

Acknowledgements

The author is grateful to Dr. W. H. Cabot and Prof. J. D. Ramshaw for their assistance and comments. This work was performed under the auspices of the U.S. Department of Energy by Lawrence Livermore National Laboratory under Contract DE-AC52-07NA27344.

6 Appendix A: Numerical Algorithm

6.1 Artificial Fluid Properties

The essential feature of our LES method is the addition of grid-dependent components to the molecular transport coefficients, i.e.,

$$\mu = \mu_{\mathcal{F}} + \mu^* \ , \tag{35}$$

$$\beta = \beta_{\mathcal{F}} + \beta^* \ , \tag{36}$$

$$\kappa = \kappa_{\mathcal{F}} + \kappa^* \ , \tag{37}$$

$$D_i = D_{\mathcal{F},i} + D_i^* \ , \tag{38}$$

where the $\mathcal{F}$ subscripts denote physical fluid properties and the asterisks denote artificial properties. The artificial properties are

$$\mu^* = \overline{C_\mu \rho \left| \nabla^r S \right| \Delta^{(r+2)}} \ , \tag{39}$$

$$\beta^* = \overline{C_\beta \rho \left| \nabla^r S \right| \Delta^{(r+2)}} \ , \tag{40}$$

$$\kappa^* = \overline{C_\kappa \rho |e|^{3/2} \left| \nabla^r T \right| \Delta^{(r+1)} / T^2} \ , \tag{41}$$

$$D_i^* = \overline{\{ C_D |\nabla^r (\nabla Y_i \cdot \nabla Y_i)| \Delta^{(r+2)} + C_Y (|Y_i| - 1 + |1 - Y_i|) \} \, \Delta^2 / \Delta t} \ , \tag{42}$$

where $S = (\underline{\mathbf{S}} : \underline{\mathbf{S}})^{1/2}$ is the magnitude of the strain rate tensor, $\Delta = (\Delta x \Delta y \Delta z)^{1/3}$ is the local grid spacing and Δt is the time step. The polyharmonic operator, ∇^r, denotes a series of Laplacians, e.g., $r = 4$ (used for the simulations herein) corresponds to the biharmonic operator, $\nabla^4 = \nabla^2 \nabla^2$.

The overbar ($\overline{f}$) denotes a truncated-Gaussian filter, defined as

$$\overline{f}(\mathbf{x}) = \int_{-L}^{L} G(|\mathbf{x} - \boldsymbol{\xi}|; L) f(\boldsymbol{\xi}) d^3\xi \ , \tag{43}$$

where

$$G(\zeta; L) = \frac{e^{-6\zeta^2/L^2}}{\int_{-L}^{L} e^{-6\zeta^2/L^2} d\zeta} \ , \quad L = 4\Delta \ . \tag{44}$$

This filter eliminates cusps introduced by the absolute value operators, which in turn, ensure that the artificial properties are positive definite. On Cartesian grids, (43) is applied sequentially along each grid line (with nodal index j) as

$$\begin{aligned}\overline{f}_j = \frac{3565}{10368} f_j + \frac{3091}{12960}(f_{j-1} + f_{j+1}) + \frac{1997}{25920}(f_{j-2} + f_{j+2}) \\ + \frac{149}{12960}(f_{j-3} + f_{j+3}) + \frac{107}{103680}(f_{j-4} + f_{j+4}) \ .\end{aligned} \tag{45}$$

The empirical constants appearing in (35)-(38) are: $C_\mu = 0.002$, $C_\beta = 1$, $C_\kappa = 0.01$, $C_D = 0.001$ and $C_Y = 50$. The artificial terms are designed to vanish wherever the flow is sufficiently smooth with respect to the grid scale. The efficacy of this LES method has been established both theoretically [18] and in practice [19, 20].

6.2 Spatial Differencing

The governing equations are solved in fully conservative form. All first derivatives, comprising the gradient and divergence operators, are computed according to the 10th-order compact scheme [21]

$$\beta f'_{j-2} + \alpha f'_{j-1} + f'_j + \alpha f'_{j+1} + \beta f'_{j+2}$$

$$= a\frac{f_{j+1} - f_{j-1}}{2\Delta} + b\frac{f_{j+2} - f_{j-2}}{4\Delta} + c\frac{f_{j+3} - f_{j-3}}{6\Delta} \ , \tag{46}$$

where f'_j represents the derivative of f at node j, Δ is the spacing between nodes and

$$\alpha = \frac{1}{2} \, , \ \beta = \frac{1}{20} \, , \ a = \frac{17}{12} \, , \ b = \frac{101}{150} \, , \ c = \frac{1}{100} \ .$$

Similarly, all second derivatives (f''_j), comprising the polyharmonic operators in the artificial fluid properties, are computed according to the 10th-order compact scheme

$$\beta f''_{j-2} + \alpha f''_{j-1} + f''_j + \alpha f''_{j+1} + \beta f''_{j+2}$$

$$= a\frac{f_{j+1} - 2f_j + f_{j-1}}{\Delta^2} + b\frac{f_{j+2} - 2f_j + f_{j-2}}{4\Delta^2} + c\frac{f_{j+3} - 2f_j + f_{j-3}}{9\Delta^2} \ , \tag{47}$$

where

$$\alpha = \frac{334}{899} \, , \ \beta = \frac{43}{1798} \, , \ a = \frac{1065}{1798} \, , \ b = \frac{1038}{899} \, , \ c = \frac{79}{1798} \ .$$

6.3 Temporal Integration

The governing equations are advanced in time by casting them all in the form $\dot{\Phi} = F$ and integrating via a five-step 4th-order Runge-Kutta (RK4) method [22]. The scheme is

$$\begin{aligned} Q^{\eta} &= \Delta t F^{\eta-1} + A^{\eta} Q^{\eta-1} \\ & \qquad\qquad\qquad\qquad \eta = 1, ..., 5 \\ \Phi^{\eta} &= \Phi^{\eta-1} + B^{\eta} Q^{\eta} \end{aligned} \tag{48}$$

where Δt is the time step, η is the RK4 subcycle, and A^{η} and B^{η} are:

$$\begin{aligned}
A^1 &= 0 \\
A^2 &= -6234157559845/12983515589748 \\
A^3 &= -6194124222391/4410992767914 \\
A^4 &= -31623096876824/15682348800105 \\
A^5 &= -12251185447671/11596622555746 \\
B^1 &= 494393426753/4806282396855 \\
B^2 &= 4047970641027/5463924506627 \\
B^3 &= 9795748752853/13190207949281 \\
B^4 &= 4009051133189/8539092990294 \\
B^5 &= 1348533437543/7166442652324 \ .
\end{aligned}$$

The fraction of Δt for which the solution advances after each substep is:

$$\begin{aligned}
&\eta = 1 \Rightarrow 494393426753/4806282396855 \\
&\eta = 2 \Rightarrow 4702696611523/9636871101405 \\
&\eta = 3 \Rightarrow 3614488396635/5249666457482 \\
&\eta = 4 \Rightarrow 9766892798963/10823461281321 \\
&\eta = 5 \Rightarrow 1 \ .
\end{aligned}$$

Partial de-aliasing is accomplished by applying an 8th-order compact filter to the conserved variables ρY_i, $\rho\mathbf{u}$ and E after each RK4 substep. The compact filter is designed to remove the top one-tenth of the wavenumbers in as sharp a manner as possible, such that results remain independent of the frequency of filter application (which depends on Δt). The filter stencil is

$$\begin{aligned}\beta\hat{f}_{j-2}+\alpha\hat{f}_{j-1}+\hat{f}_j+\alpha\hat{f}_{j+1}+\beta\hat{f}_{j+2} &= af_j+\frac{b}{2}(f_{j-1}+f_{j+1}) \\ &+\frac{c}{2}(f_{j-2}+f_{j+2})+\frac{d}{2}(f_{j-3}+f_{j+3})+\frac{e}{2}(f_{j-4}+f_{j+4}) \quad , \qquad (49)\end{aligned}$$

where $\hat{f}_j$ is the filtered variable and

$$\alpha=0.66624\ ,\quad \beta=0.16688\ ,\quad a=0.99965\ ,\quad \frac{b}{2}=0.66652 \qquad (50)$$

$$\frac{c}{2}=0.16674\ ,\quad \frac{d}{2}=4\times10^{-5}\ ,\quad \frac{e}{2}=-5\times10^{-6}\ . \qquad (51)$$

This compact filter helps prevent the artificial fluid properties from becoming too large. For example, without this filter, β^* can become extremely large in the vicinity of strong shocks, thus driving the viscously stable timestep to zero and bringing the simulation to a halt.

6.4 Stability

The maximum stable time step is limited not only by the inviscid CFL condition [23],

$$\Delta t_{CFL}=\mathrm{MIN}\left(\frac{|u|}{\Delta x}+\frac{|v|}{\Delta y}+\frac{|w|}{\Delta z}+c_s\sqrt{\frac{1}{\Delta x^2}+\frac{1}{\Delta y^2}+\frac{1}{\Delta z^2}}\right)^{-1} \quad , \qquad (52)$$

where c_s is sound speed and $(u,v,w)=\mathbf{u}$, but also by the maximum viscosity, conductivity and diffusivity existing in the domain. Time scales associated with μ, β, κ and D_i are:

$$\Delta t_\mu = \mathrm{MIN}\left(\frac{\rho\Delta^2}{\mu}\right) \ , \tag{53}$$

$$\Delta t_\beta = \mathrm{MIN}\left(\frac{\rho\Delta^2}{\beta}\right) \ , \tag{54}$$

$$\Delta t_\kappa = \mathrm{MIN}\left(\frac{\rho\Delta^4}{\kappa T}\right)^{1/3} \ , \tag{55}$$

$$\Delta t_D = \mathrm{MIN}\left(\frac{\Delta^2}{D_i}\right) \ . \tag{56}$$

The simulation time step is chosen to be

$$\Delta t = \mathrm{MIN}(\Delta t_{CFL}, 0.2\Delta t_\mu, 0.2\Delta t_\beta, 0.2\Delta t_\kappa, 0.2\Delta t_D) \ . \tag{57}$$

7 Appendix B: Mixture Formulas for Tabular Equations of State

7.1 Pressure/Temperature Equilibration

The purpose of the mixture equation of state is to provide p, T and h_i as functions of ρ, e and Y_i. In ICF and astrophysical applications, as well as other problems where pressures and temperatures span a very broad range, equations of state for the various materials are often given by tables. These tables typically provide material-specific thermodynamic quantities as functions of species density and species temperature; e.g., $p_i = p_i(\rho_i, T_i)$. An inverse option is usually available to look up temperature as a function of density and internal energy; i.e., $T_i = T_i(\rho_i, e_i)$. Additionally, the tables usually provide partial derivatives of the output variables with respect to the input variables. In applying these tables to mixed regions of the flow, an iterative procedure can be employed, whereby the various species are all equilibrated to the same temperature and pressure. Pressure equilibration is strictly valid only for neutral (nonionized) gases. For partially or fully ionized plasma mixtures, equating electron number densities or chemical potentials, instead of pressures, yields more accurate results [24]. Since tables of chemical potentials are less commonly available than pressure tables, the iterative algorithm below is given in terms of pressure equilibration. However, the same algorithm could also be used to equilibrate chemical potentials.

Species pressures are related to the mixture pressure by

$$\sum_{i=1}^{N} v_i \, p_i = p \; , \tag{58}$$

where

$$v_i = \rho Y_i / \rho_i \tag{59}$$

is the volume fraction of species i. In an ideal solution, a volume fraction is the portion of a grid cell that a species would occupy if all of its molecules were gathered together in one place; i.e., as if imaginary partitions separated each of the species present in a cell. If each subvolume exists at the same pressure and temperature, then there will be no tendency for the partitions to move. With these constraints on the solution, the thermodynamic state equations to be solved are:

$$p_i(\rho_i, T_i) = p \ , \tag{60}$$

$$T_i(\rho_i, e_i) = T \ , \tag{61}$$

$$\sum_{i=1}^{N} Y_i \xi_i = \xi \ , \tag{62}$$

$$\sum_{i=1}^{N} Y_i e_i = e \ ; \tag{63}$$

where $\xi_i = 1/\rho_i$ is the specific volume of material i and $\xi = 1/\rho$ is the specific volume of the mixture as a whole. Equations (60)-(63) constitute $2N + 2$ equations in the $2N + 2$ unknowns: ξ_i, e_i, p and T.

7.2 Solution via Newton Iteration

In solving for ξ_i, e_i, p and T, the procedure described below has been tested on a wide variety of problems, including cases with materials undergoing phase changes from solid to gas to plasma. It has been found to be very robust and to converge rapidly at high temperatures, usually in a single iteration. It is similar to an algorithm derived by Cranfill [25].

Beginning with guesses for the specific volumes (ξ_i^η) and species energies (e_i^η), changes in ξ_i and e_i from iteration η to iteration $\eta+1$ are expressed by the linearized Taylor series expansions:

$$\delta\xi_i^{\eta+1} \equiv \xi_i^{\eta+1} - \xi_i^\eta = \left.\frac{\partial\xi_i}{\partial p_i}\right|_{T_i}^{\eta} (p^{\eta+1} - p_i^\eta) + \left.\frac{\partial\xi_i}{\partial T_i}\right|_{p_i}^{\eta} (T^{\eta+1} - T_i^\eta) \ , \tag{64}$$

$$\delta e_i^{\eta+1} \equiv e_i^{\eta+1} - e_i^\eta = \left.\frac{\partial e_i}{\partial p_i}\right|_{T_i}^{\eta} (p^{\eta+1} - p_i^\eta) + \left.\frac{\partial e_i}{\partial T_i}\right|_{p_i}^{\eta} (T^{\eta+1} - T_i^\eta) \ , \tag{65}$$

wherein $p_i^{\eta+1}$ and $T_i^{\eta+1}$ have been replaced by $p^{\eta+1}$ and $T^{\eta+1}$, respectively. This substitution is made in order to satisfy (60) and (61). We further require $\xi_i^{\eta+1}$ and $e_i^{\eta+1}$ to satisfy (62) and (63); i.e.,

$$\sum_{i=1}^{N} Y_i \xi_i^{\eta+1} = \xi \ , \tag{66}$$

$$\sum_{i=1}^{N} Y_i e_i^{\eta+1} = e \ . \tag{67}$$

Equations (64)-(67) now constitute a determinate system of $2N+2$ equations in the $2N+2$ unknowns: $\xi_i^{\eta+1}$, $e_i^{\eta+1}$, $p^{\eta+1}$ and $T^{\eta+1}$.

Substituting (64) and (65) into (66) and (67) yields:

$$A_{pp} p^{\eta+1} + A_{pT} T^{\eta+1} = B_p \ , \tag{68}$$

$$A_{Tp} p^{\eta+1} + A_{TT} T^{\eta+1} = B_T \ , \tag{69}$$

where

$$A_{pp} = \sum_{i=1}^{N} \rho Y_i \left.\frac{\partial\xi_i}{\partial p_i}\right|_{T_i}^{\eta} \ , \tag{70}$$

$$A_{pT} = \sum_{i=1}^{N} \rho Y_i \left. \frac{\partial \xi_i}{\partial T_i} \right|_{p_i}^{\eta} , \tag{71}$$

$$A_{Tp} = \sum_{i=1}^{N} Y_i \left. \frac{\partial e_i}{\partial p_i} \right|_{T_i}^{\eta} , \tag{72}$$

$$A_{TT} = \sum_{i=1}^{N} Y_i \left. \frac{\partial e_i}{\partial T_i} \right|_{p_i}^{\eta} , \tag{73}$$

$$B_p = 1 - \sum_{i=1}^{N} \rho Y_i \xi_i^{\eta} + \sum_{i=1}^{N} \rho Y_i \left[p_i^{\eta} \left. \frac{\partial \xi_i}{\partial p_i} \right|_{T_i}^{\eta} + T_i^{\eta} \left. \frac{\partial \xi_i}{\partial T_i} \right|_{p_i}^{\eta} \right] , \tag{74}$$

$$B_T = e - \sum_{i=1}^{N} Y_i e_i^{\eta} + \sum_{i=1}^{N} Y_i \left[p_i^{\eta} \left. \frac{\partial e_i}{\partial p_i} \right|_{T_i}^{\eta} + T_i^{\eta} \left. \frac{\partial e_i}{\partial T_i} \right|_{p_i}^{\eta} \right] . \tag{75}$$

Solving (68) and (69) for $p^{\eta+1}$ and $T^{\eta+1}$ yields

$$p^{\eta+1} = \frac{A_{TT} B_p - A_{pT} B_T}{A_{pp} A_{TT} - A_{pT} A_{Tp}} , \tag{76}$$

$$T^{\eta+1} = \frac{A_{pp} B_T - A_{Tp} B_p}{A_{pp} A_{TT} - A_{pT} A_{Tp}} . \tag{77}$$

The recipe for iteration is as follows:

(i) Guess starting values ($\eta = 0$) for the individual specific volumes ($\xi_i^{\eta} = 1/\rho_i^{\eta}$) and species energies ($e_i^{\eta}$). These values are ordinarily taken from the previous timestep or from known initial conditions.

(ii) Query the EOS tables (inverse option) to obtain $T_i^{\eta}(\rho_i^{\eta}, e_i^{\eta})$, $\partial e_i/\partial T_i|_{\rho_i}^{\eta}$ and $\partial e_i/\partial \rho_i|_{T_i}^{\eta}$. For certain problems involving phase changes, it has been found helpful to apply a floor to the species temperatures; i.e., to ensure that $T_i^{\eta} \geq T_{\min}$, where $T_{\min}$ is a temperature below which the solution should not extend.

(iii) Query the EOS tables to obtain $p_i^{\eta}(\rho_i^{\eta}, T_i^{\eta})$, $\partial p_i/\partial T_i|_{\rho_i}^{\eta}$ and $\partial p_i/\partial \rho_i|_{T_i}^{\eta}$. For certain problems involving phase changes, it has been found necessary to apply a floor to both the species pressures and their partial derivatives with respect to density; i.e., to ensure that $p_i^\eta \geq p_{\min}$ and $\partial p_i/\partial\rho_i|_{T_i}^\eta \geq p_{\min}/\rho_i^\eta$, where $p_{\min}$ is a positive floor pressure. This avoids divisions by zero in steps (iv) and (v).

(iv) Check for convergence by computing

$$\epsilon_{p,i}^\eta = |Y_i(p_i^\eta - p^\eta)/p^\eta| \ , \tag{78}$$

$$\epsilon_{T,i}^\eta = |Y_i(T_i^\eta - T^\eta)/T^\eta| \ . \tag{79}$$

If all $\epsilon_{p,i}^\eta < \epsilon_p$ and all $\epsilon_{T,i}^\eta < \epsilon_T$, where $\epsilon_p = \epsilon_T \approx 10^{-5}$, then exit iteration; otherwise, continue to step (v).

(v) Compute the following derivatives [26]:

$$\left.\frac{\partial\rho_i}{\partial p_i}\right|_{T_i}^\eta = 1/\left.\frac{\partial p_i}{\partial\rho_i}\right|_{T_i}^\eta \ , \tag{80}$$

$$\left.\frac{\partial\rho_i}{\partial T_i}\right|_{p_i}^\eta = -\left.\frac{\partial\rho_i}{\partial p_i}\right|_{T_i}^\eta \left.\frac{\partial p_i}{\partial T_i}\right|_{\rho_i}^\eta \ , \tag{81}$$

$$\left.\frac{\partial e_i}{\partial p_i}\right|_{T_i}^\eta = \left.\frac{\partial e_i}{\partial\rho_i}\right|_{T_i}^\eta \left.\frac{\partial\rho_i}{\partial p_i}\right|_{T_i}^\eta \ , \tag{82}$$

$$\left.\frac{\partial e_i}{\partial T_i}\right|_{p_i}^\eta = \left.\frac{\partial e_i}{\partial T_i}\right|_{\rho_i}^\eta + \left.\frac{\partial e_i}{\partial\rho_i}\right|_{T_i}^\eta \left.\frac{\partial\rho_i}{\partial T_i}\right|_{p_i}^\eta \ , \tag{83}$$

$$\left.\frac{\partial\xi_i}{\partial p_i}\right|_{T_i}^\eta = -\frac{1}{(\rho_i^\eta)^2}\left.\frac{\partial\rho_i}{\partial p_i}\right|_{T_i}^\eta \ , \tag{84}$$

$$\left.\frac{\partial\xi_i}{\partial T_i}\right|_{p_i}^\eta = -\frac{1}{(\rho_i^\eta)^2}\left.\frac{\partial\rho_i}{\partial T_i}\right|_{p_i}^\eta \ . \tag{85}$$

(vi) Evaluate $p^{\eta+1}$ and $T^{\eta+1}$ using (76) and (77).

(vii) Evaluate $\delta\xi_i^{\eta+1}$ and $\delta e_i^{\eta+1}$ using (64) and (65).

(viii) Apply limiters to the changes in volumes and energies; i.e.,

$$\delta\xi_i^* = MIN(\delta\xi_i^{\eta+1}, \delta\xi_i^{\max}) \;, \tag{86}$$

$$\delta\xi_i^{**} = MAX(\delta\xi_i^*, \delta\xi_i^{\min}) \;, \tag{87}$$

$$\delta e_i^* = MIN(\delta e_i^{\eta+1}, \delta e_i^{\max}) \;, \tag{88}$$

$$\delta e_i^{**} = MAX(\delta e_i^*, \delta e_i^{\min}) \;; \tag{89}$$

where

$$\delta\xi_i^{\max} = (s_\xi - 1)\xi_i^\eta \;, \tag{90}$$

$$\delta\xi_i^{\min} = (1/s_\xi - 1)\xi_i^\eta \;, \tag{91}$$

$$\delta e_i^{\max} = (s_e - 1)e_i^\eta \;, \tag{92}$$

$$\delta e_i^{\min} = (1/s_e - 1)e_i^\eta \;. \tag{93}$$

The limiters, s_ξ and s_e, are typically each set to 2.0.

(ix) Compute $\xi_i^{\eta+1} = \xi_i^\eta + \delta\xi_i^{**}$, $\rho_i^{\eta+1} = 1/\xi_i^{\eta+1}$ and $e_i^{\eta+1} = e_i^\eta + \delta e_i^{**}$.

(x) Increment η and return to step (ii).

Once the iteration is complete, the species enthalpies can be computed from (13).

7.3 Practical Considerations

In order to reduce the EOS workload, the Newton iteration described above need only be applied to those materials that are actually present within a zone.

Unfortunately, this allows the temperatures and pressures of the materials not computed to gradually drift away from the mixture pressure and temperature of the zone. Thus when a material first enters a new zone, the initial guess for its specific volume and energy may be outside the radius of convergence of the Taylor's series. Furthermore, sometimes one or more materials in the vicinity of phase boundaries, in the EOS tables, will fail to converge to the mixture temperature and/or pressure of a zone. Both of these problems can be alleviated by assigning $p_i = p$ and $T_i = T$ after each complete timestep and then updating ρ_i and e_i to be consistent with the pressure and temperature of each zone (the ρ_i update requires a trivial iteration). This ensures good guesses for all materials in all zones at the beginning of every iteration. This equilibration procedure is justified, to some extent, by the fact that for neutral (nonionized) ideal gases the mixture pressure (58) does not depend on the subvolume pressures being equal [24].

References

[1] P. F. Linden, J. M. Redondo, and D. L. Youngs. Molecular mixing in Rayleigh-Taylor instability. *J. Fluid Mech.*, 265:97–124, 1994.

[2] D. L. Youngs. Numerical simulation of mixing by Rayleigh-Taylor and Richtmyer-Meshkov instabilities. *Laser and Particle Beams*, 12:725–750, 1994.

[3] R. Abgrall and S. Karni. Computations of compressible multifluids. *J. Comput. Phys.*, 169:594–623, 2001.

[4] A. Marquina and P. Mulet. A flux-split algorithm applied to conservative models for multicomponent compressible flows. *J. Comput. Phys.*, 185:120–138, 2003.

[5] P. Jenny, B. Müller, and H. Thomann. Correction of conservative Euler solvers for gas mixtures. *J. Comput. Phys.*, 132:91–107, 1997.

[6] C. Mügler and S. Gauthier. Two-dimensional Navier-Stokes simulations of gaseous mixtures induced by Richtmyer-Meshkov instability. *Phys. Fluids*, 12:1783–1798, 2000.

[7] D. J. Hill, C. Pantano, and D. I. Pullin. Large-eddy simulation and multiscale modelling of a Richtmyer-Meshkov instability with reshock. *J. Fluid Mech.*, 557:29–61, 2006.

[8] G. Dimonte and R. Tipton. K-L turbulence model for the self-similar growth of the Rayleigh-Taylor and Richtmyer-Meshkov instabilities. *Phys. Fluids*, 18:085101, 2006.

[9] K. R. Bates, N. Nikiforakis, and D. Holder. Richtmyer-Meshkov instability induced by the interaction of a shock wave with a rectangular block of SF6. *Phys. Fluids*, 19:036101, 2007.

[10] C. Pantano, R. Deiterding, D. J. Hill, and D. I. Pullin. A low numerical

dissipation patch-based adaptive mesh refinement method for large-eddy simulation of compressible flows. *J. Comput. Phys.*, 221:63–87, 2007.

[11] H. Lim, Y. Yu, H. Jin, D. Kim, H. Lee, J. Glimm, X.-L. Li, and D. H. Sharp. Multiscale models for fluid mixing. *Comput. Methods Appl. Mech. Engrg.*, 197:3435–3444, 2008.

[12] J. O. Hirschfelder, C. F. Curtiss, and R. B. Bird. *Molecular Theory of Gases and Liquids*. Wiley, New York, 1954.

[13] R. B. Bird, W. E. Stewart, and E. N. Lightfoot. *Transport Phenomena*. John Wiley and Sons, 1960.

[14] F. A. Williams. *Combustion Theory 2nd ed.* Addison-Wesley, 1985.

[15] J. D. Ramshaw. Fluid dynamics and energetics in ideal gas mixtures. *Am. J. Phys.*, 70:508–512, 2002.

[16] J.-F. Haas and B. Sturtevant. Interaction of weak shock waves with cylindrical and spherical gas inhomogeneities. *J. Fluid Mech.*, 181:41–76, 1987.

[17] J.J. Quirk and S. Karni. On the dynamics of a shock-bubble interaction. *J. Fluid Mech.*, 318:129–163, 1996.

[18] A. W. Cook and W. H. Cabot. A high-wavenumber viscosity for high-resolution numerical methods. *J. Comput. Phys.*, 195:594–601, 2004.

[19] A. W. Cook and W. H. Cabot. Hyperviscosity for schock-turbulence interactions. *J. Comput. Phys.*, 203:379–385, 2005.

[20] A. W. Cook. Artificial fluid properties for large-eddy simulation of compressible turbulent mixing. *Phys. Fluids*, 19:055103, 2007.

[21] S. K. Lele. Compact finite difference schemes with spectral-like resolution. *J. Comput. Phys.*, 103:16–42, 1992.

[22] C. A. Kennedy, M. H. Carpenter, and R. M. Lewis. Low-storage, explicit Runge-Kutta schemes for the compressible Navier-Stokes equations.

35:177–219, 2000.

[23] D. A. Anderson, J. C. Tannehill, and R. H. Pletcher. *Computational Fluid Mechanics and Heat Transfer*. Hemisphere Publishing Corporation, 1984.

[24] J. D. Ramshaw. Approximate thermodynamic state relations in partially ionized gas mixtures. *Phys. Plasmas*, 11:3572–3578, 2004.

[25] C. W. Cranfill. EOS of a material mixture in pressure equilibrium. Los Alamos National Laboratory Report No. LA-13661, 2000.

[26] L. E. Reichl. *A Modern Course in Statistical Physics*. John Wiley and Sons, Inc., New York, N.Y., 1998.